Energy Materials

Supplementary Materials

Exsolved nickel sites for methane decomposition to hydrogen and carbon

Song Rong Chua[1,#], Ruinan Wang[2,#], Zhihua Deng[1,3], Guoping Xiao[4], Jian-Qiang Wang[4], Hongquan He[5], Xun Cao[5], Chee Kok Poh[5], Lili Zhang[1,5], Lan Zhang[3,4,*], Meng Ni[2,*], Siew Hwa Chan[1,3,*]

[1]School of Mechanical and Aerospace Engineering, Nanyang Technological University, Singapore 639798, Singapore.
[2]Department of Building Environment and Energy Engineering, Research Institute for Sustainable Urban Development (RISUD) and Research Institute for Smart Energy (RISE), The Hong Kong Polytechnic University, Hong Kong 999077, China.
[3]Energy Research Institute at NTU (ERI@N), Nanyang Technological University, Singapore 637141, Singapore.
[4]State Key Laboratory of Thorium Energy, Shanghai Institute of Applied Physics, Chinese Academy of Sciences, Shanghai 201800, China.
[5]Institute of Sustainability for Chemicals, Energy and Environment (ISCE2), Agency for Science, Technology and Research (A*STAR), Singapore 627833, Singapore.
[#]These authors contributed equally to this work.

[*]**Correspondence to:** Prof. Lan Zhang, Energy Research Institute at NTU (ERI@N), Nanyang Technological University, Singapore 637141, Singapore; State Key Laboratory of Thorium Energy, Shanghai Institute of Applied Physics, Chinese Academy of Sciences, Shanghai 201800, China. E-mail: zhanglan5678@sinap.ac.cn; Prof. Meng Ni, Department of Building Environment and Energy Engineering, Research Institute for Sustainable Urban Development (RISUD) and Research Institute for Smart Energy (RISE), The Hong Kong Polytechnic University, Hong Kong 999077, China. E-mail: meng.ni@polyu.edu.hk; Prof. Siew Hwa Chan, School of Mechanical and Aerospace Engineering, Nanyang Technological University, Singapore 639798, Singapore; Energy Research Institute at NTU (ERI@N), Nanyang Technological University, Singapore 637141, Singapore. E-mail: mshchan@ntu.edu.sg

ORCID: Song Rong Chua (0009-0008-2417-4773), Ruinan Wang (0000-0002-9576-6038), Zhihua Deng (0000-0002-4305-1559), Guoping Xiao (0000-0003-4353-913X), Jian-Qiang Wang (0000-0003-4123-7592), Lili Zhang (0000-0002-9143-9320), Lan Zhang (0000-0003-3675-1124), Meng Ni (0000-0001-5310-4039), Siew Hwa Chan (0000-0003-0753-0488)

Table S1. ICP-OES-derived molar ratios calculated from measured elemental concentrations and normalized to La = 0.75

050Ni–LCCM	Ni	La	Ca	Cr	Mn
Expected	0.50	0.75	0.25	0.50	0.50
Batch 1	0.45	0.75	0.21	0.43	0.47
Batch 2	0.44	0.75	0.21	0.44	0.46
Batch 3	0.44	0.75	0.21	0.44	0.46

The measured ICP-OES concentrations were converted to molar values using the respective molar masses. To account for minor dilution variations arising from pipetting and sample preparation, the molar ratio of each batch was normalized to La = 0.75, corresponding to the targeted La content in 050Ni–LCCM.

Table S2. Comparison of carbon yield determined from collected carbon mass and from thermogravimetric analysis (TGA) for representative Ni–LCCM catalysts, where TGA was performed on carbon obtained from the same experimental run

Catalyst	Carbon yield ($g_C \cdot g_{cat.}^{-1}$)	Carbon yield from TGA ($g_C \cdot g_{cat.}^{-1}$)
050Ni–LCCM	1.38	1.42
150Ni–LCCM	3.05	3.28
175Ni–LCCM	3.25	3.36
200Ni–LCCM	3.39	3.66

Table S3 Comparison of carbon productivity and reaction conditions for xNi–LCCM catalysts and representative Ni-based methane decomposition catalysts reported in the literature

Catalyst	Active metal content (wt%)	Space velocity ($L \cdot g_{cat.}^{-1} \cdot h^{-1}$)	CH_4 conversion (%)	Feed	Time (min)	Carbon yield	T_r (°C)	Reduction	Ref.
050Ni–LCCM	12	3	34 → 3	CH_4	480	11.5 $g_C \cdot g_{Ni}^{-1}$	750	No	This work
150Ni–LCCM	27		41 → 23			11.1 $g_C \cdot g_{Ni}^{-1}$			
Ni/MgO	20	9	-	CH_4	360	6.1 $g_C \cdot g_{Ni}^{-1}$	700	700 °C ,1.5h	[1]
						8.6 $g_C \cdot g_{Ni}^{-1}$	800		
						9.3 $g_C \cdot g_{Ni}^{-1}$	900		
UI-Ni/SiO_2	10	15	29 → 0[a]	CH_4	120	11.7 $g_C \cdot g_{Ni}^{-1}$	550	550 °C ,0.5h	[2]
I-Ni/SiO_2			24 → 9[a]			26.4 $g_C \cdot g_{Ni}^{-1}$			
Ni/mSiO_2	10	24	12	90% CH_4	60	13.8 $g_C \cdot g_{Ni}^{-1}$	600	Yes	[3]
Ni0.2Zr/mSiO_2			23			25.4 $g_C \cdot g_{Ni}^{-1}$ [b]			
Ni0.2Zr/mSiO_2			28 → 15[a]	40% CH_4	300	6.4 $g_C \cdot g_{Ni}^{-1}$ [b]			
10Ni/MCM-41	10	12	65 → 3[a]	40% CH_4	240	5.0 $g_C \cdot g_x^{-1}$	550	550 °C ,1h	[4]
10Ni2.5Co/MCM-41			68			13.1 $g_C \cdot g_x^{-1}$			
$LaNiO_3$	24	-	-	CH_4	300	10.0 $g_C \cdot g_x^{-1}$	800	600 °C ,1h	[5]
$LaNi_{0.8}Co_{0.2}O_3$						10.5 $g_C \cdot g_x^{-1}$			
$LaNi_{0.8}Fe_{0.2}O_3$						11.0 $g_C \cdot g_x^{-1}$			

Ni_{10}/CeO_2	10	72	8	50% CH_4	30	0.7 $g_C \cdot g_{cat.}^{-1}$	600	500 °C ,1h	[6]
Ni_8Co_2/CeO_2			18			1.6 $g_C \cdot g_{cat.}^{-1}$			
Ni/Al_2O_3	54[c]	12	53	CH_4	180	9.8 $g_C \cdot g_{cat.}^{-1}$	700	550 °C	[7]
Ni-Cu/MgO	89[c]		61			11.5 $g_C \cdot g_{cat.}^{-1}$			
60Ni-5Mn-5Ru/Al_2O_3	70-80	36	76 → 11	CH_4	84	0.9 $g_C \cdot g_{cat.}^{-1}$	750	650 °C ,2h	[8]
60Ni-5Mn-10Ru/Al_2O_3			81 → 8		105	0.9 $g_C \cdot g_{cat.}^{-1}$			
60Ni-5Mn-15Ru/Al_2O_3			75 → 12		93	0.8 $g_C \cdot g_{cat.}^{-1}$			

T_r: Reaction temperature; a: Values represent initial to final values of CH_4 conversion over the reported reaction time; b: Did not include the Zr mass; c: Values refer to total active metal content unless otherwise specified. $g_C \cdot g_x^{-1}$: Mass of carbon produced normalized by total metal content (x).

Table S4. Elementary C–H bond cleavage steps considered for methane decomposition on catalyst surfaces

Step 1	$*CH_4 + * \rightarrow *CH_3 + *H$
Step 2	$*CH_3 + * \rightarrow *CH_2 + *H$
Step 3	$*CH_2 + * \rightarrow *CH + *H$
Step 4	$*CH + * \rightarrow *C + *H$

The asterisk (*) denotes an empty surface site. Hydrogen recombination/desorption was treated in a simplified manner and was not used to define the rate-limiting C–H activation barriers.

Table S5. Activation energies E_a for elementary methane decomposition steps on LCCM, Ni(111), and yNi–LCCM surfaces ($y = 1$–8)

E_a (eV)	$*CH_4 \rightarrow *CH_3$	$*CH_3 \rightarrow *CH_2$	$*CH_2 \rightarrow *CH$	$*CH \rightarrow *C$
LCCM	4.77	**5.88**	4.31	3.30
Ni(111)	4.17	4.62	3.60	**5.09**
1Ni–LCCM	**4.86**	2.02	3.37	1.98
2Ni–LCCM	**2.58**	1.48	2.45	0.30
3Ni–LCCM	4.15	2.69	1.48	**4.39**
4Ni–LCCM	2.17	2.54	1.80	**4.76**
5Ni–LCCM	3.57	3.33	**4.25**	3.75
6Ni–LCCM	2.85	0.51	2.95	**3.45**
7Ni–LCCM	**4.35**	3.45	4.03	3.94
8Ni–LCCM	**4.05**	2.36	3.53	2.55

The asterisk (*) denotes an empty surface site. Bold values indicate the rate-limiting step with the highest activation energy for each surface.

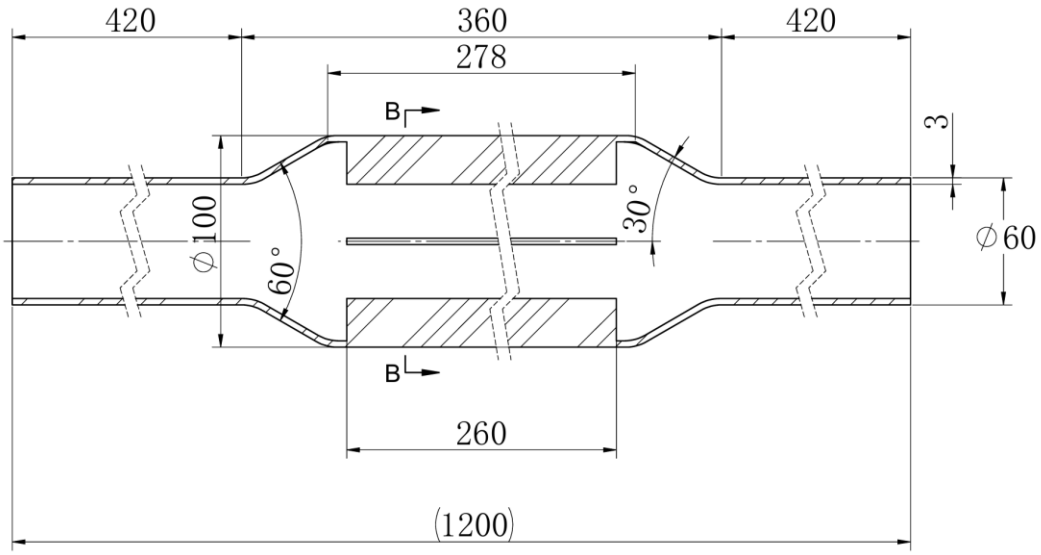

Fig. S1. CAD drawing of the specially shaped quartz tube used in the rotary-bed reactor.

Fig. S2. Photograph of the rotary-bed reactor used for CDM experiments with furnace opened, showing the quartz tube.

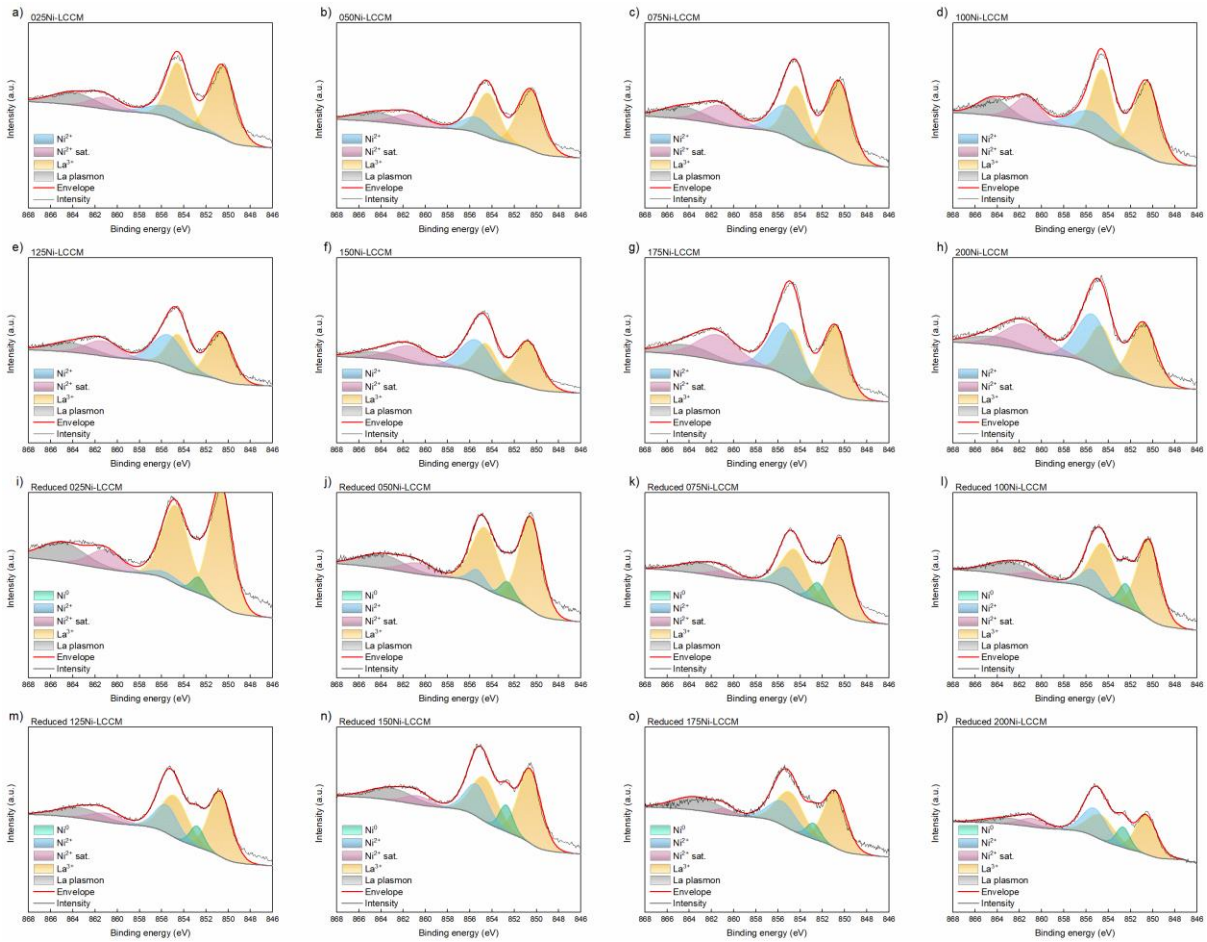

Fig. S3. Ni 2p XPS spectra of xNi-LCCM catalysts before and after reduction at 750 °C under H_2/N_2: (a) 025Ni-LCCM, (b) 050Ni-LCCM, (c) 075Ni-LCCM, (d) 100Ni-LCCM, (e) 125Ni-LCCM, (f) 150Ni-LCCM, (g) 175Ni-LCCM, and (h) 200Ni-LCCM before reduction; (i) reduced 025Ni-LCCM, (j) reduced 050Ni-LCCM, (k) reduced 075Ni-LCCM, (l) reduced 100Ni-LCCM, (m) reduced 125Ni-LCCM, (n) reduced 150Ni-LCCM, (o) reduced 175Ni-LCCM, and (p) reduced 200Ni-LCCM.

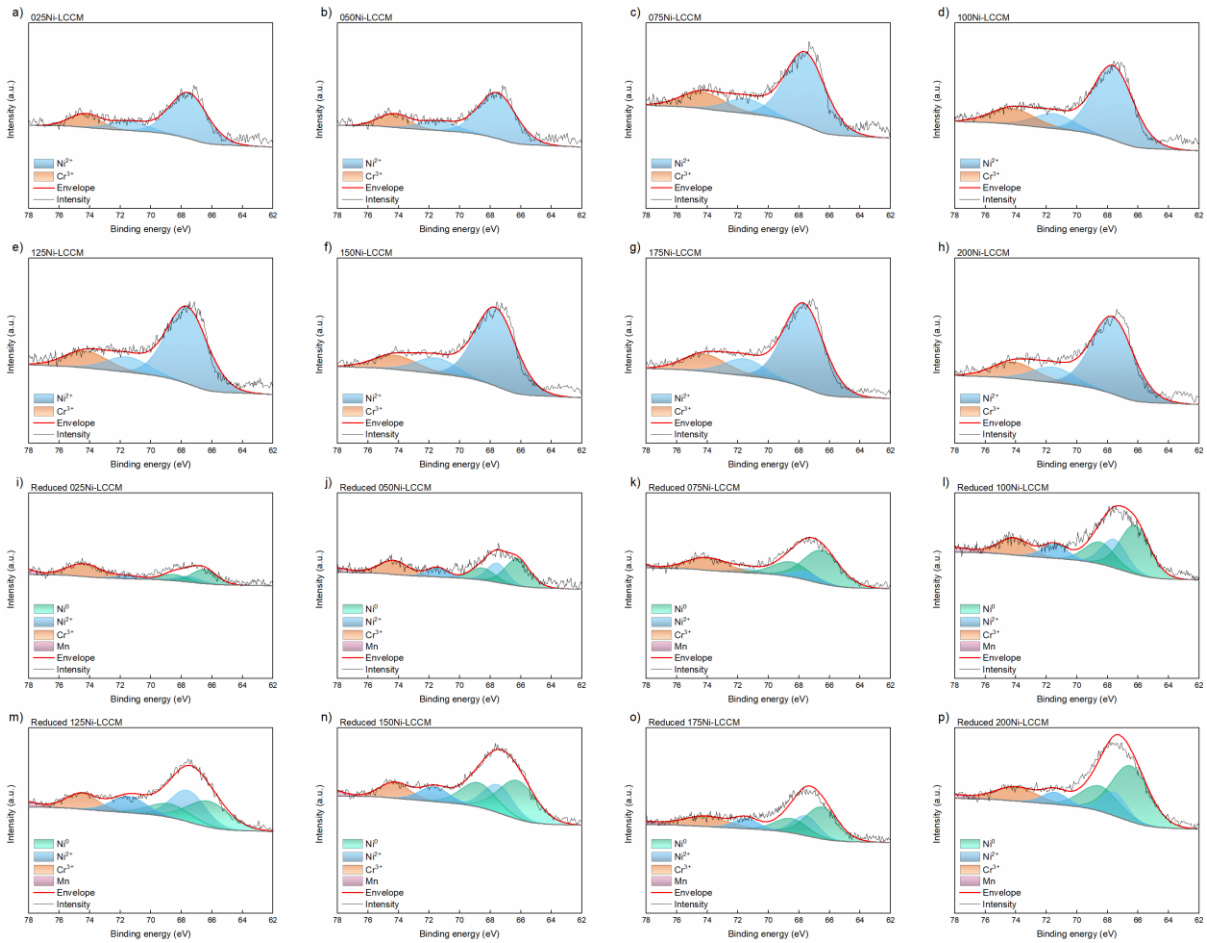

Fig. S4. Ni 3p XPS spectra of xNi-LCCM catalysts (x = 025–200) before and after reduction at 750 °C under H_2/N_2: (a) 025Ni-LCCM, (b) 050Ni-LCCM, (c) 075Ni-LCCM, (d) 100Ni-LCCM, (e) 125Ni-LCCM, (f) 150Ni-LCCM, (g) 175Ni-LCCM, and (h) 200Ni-LCCM before reduction; (i) reduced 025Ni-LCCM, (j) reduced 050Ni-LCCM, (k) reduced 075Ni-LCCM, (l) reduced 100Ni-LCCM, (m) reduced 125Ni-LCCM, (n) reduced 150Ni-LCCM, (o) reduced 175Ni-LCCM, and (p) reduced 200Ni-LCCM.

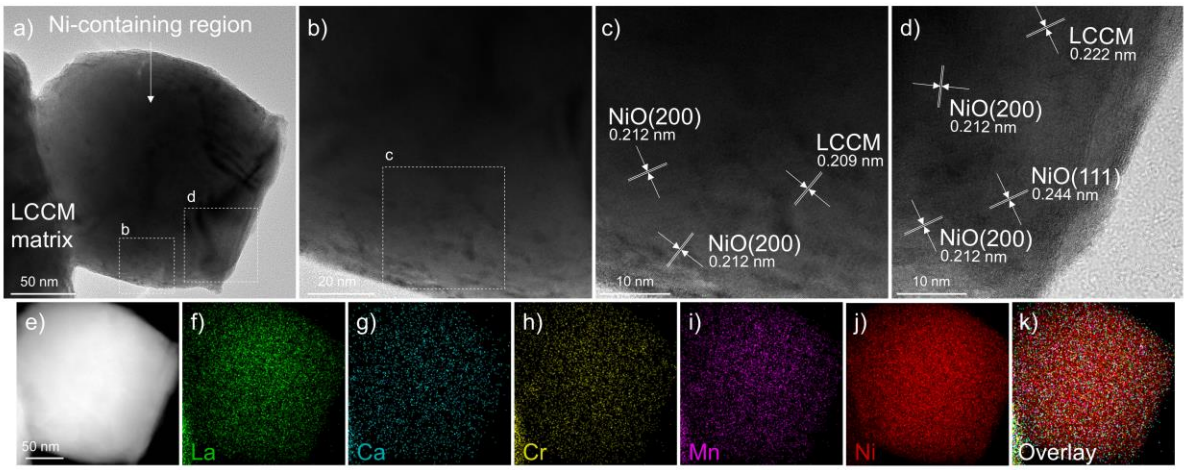

Fig. S5. (a–d) TEM, HRTEM, and STEM-EDS analysis of the 050Ni–LCCM catalyst. (a) Low-magnification TEM image showing particle morphology. (b) Enlarged TEM image of the left dashed box in (a). (c) HRTEM image enlarged from the dashed region in (b), where lattice fringes assigned to NiO(200) and the LCCM matrix are observed. (d) HRTEM image enlarged from the right dashed box in (a), showing the coexistence of NiO(111), NiO(200), and LCCM lattice fringes at the interfacial region. (e–k) STEM-EDS elemental mapping of the selected region: (e) HAADF image, (f) La, (g) Ca, (h) Cr, (i) Mn, (j) Ni, and (k) corresponding elemental overlay.

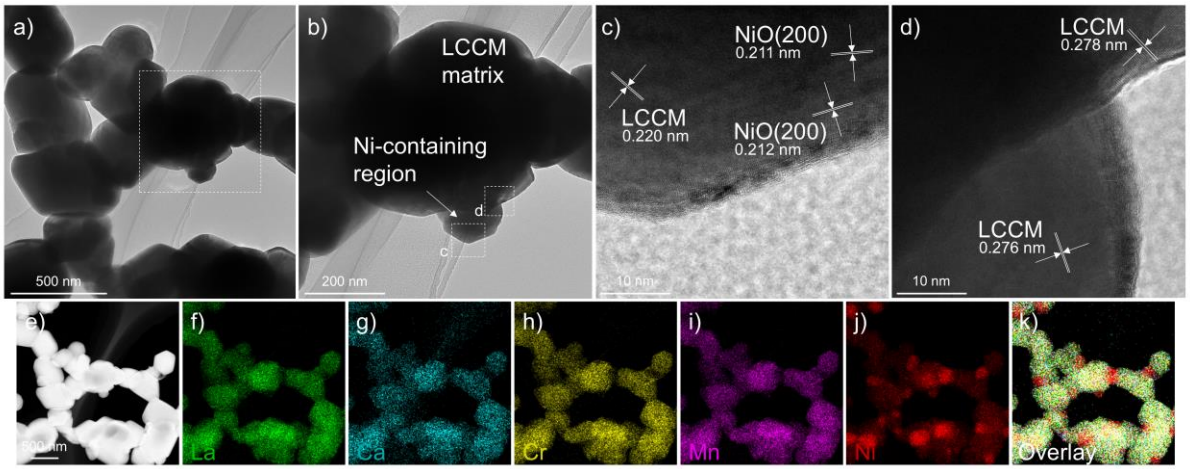

Fig. S6. (a–d) TEM, HRTEM, and STEM-EDS analysis of the 075Ni–LCCM catalyst. (a) Low-magnification TEM image showing aggregated particle morphology. (b) Enlarged TEM image of the dashed region in (a), showing a Ni-containing region at the LCCM matrix interface. (c) HRTEM image enlarged from the left dashed box in (b), where lattice fringes assigned to NiO(200) and the LCCM matrix are observed. (d) HRTEM image enlarged from the right dashed box in (b), showing LCCM lattice fringes at the interfacial region. (e–k) STEM-EDS elemental mapping of the selected region: (e) HAADF image, (f) La, (g) Ca, (h) Cr, (i) Mn, (j) Ni, and (k) corresponding elemental overlay.

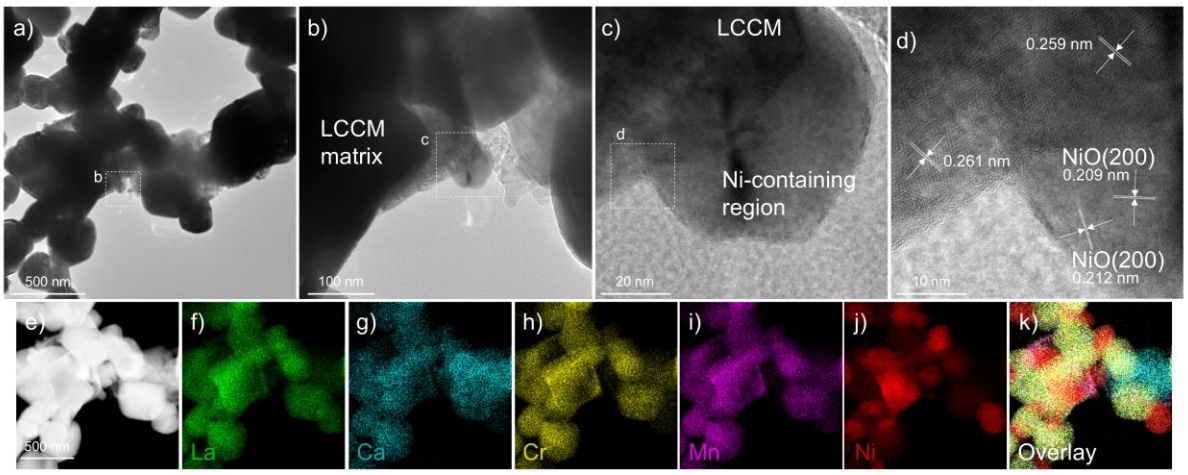

Fig. S7. (a–d) TEM, HRTEM, and STEM-EDS analysis of the 125Ni–LCCM catalyst. (a) Low-magnification TEM image showing aggregated particle morphology. (b) Enlarged TEM image of the dashed region in (a). (c) Enlarged TEM image of the dashed region in (b), showing a Ni-containing region at the LCCM matrix interface. (d) HRTEM image enlarged from the dashed box in (c), showing NiO(200) fringes together with larger spacings (~0.259–0.264 nm) observed in the surrounding oxide region, suggesting local LCCM lattice distortion near the interface. (e–k) STEM-EDS elemental mapping of the selected region: (e) HAADF image, (f) La, (g) Ca, (h) Cr, (i) Mn, (j) Ni, and (k) corresponding elemental overlay.

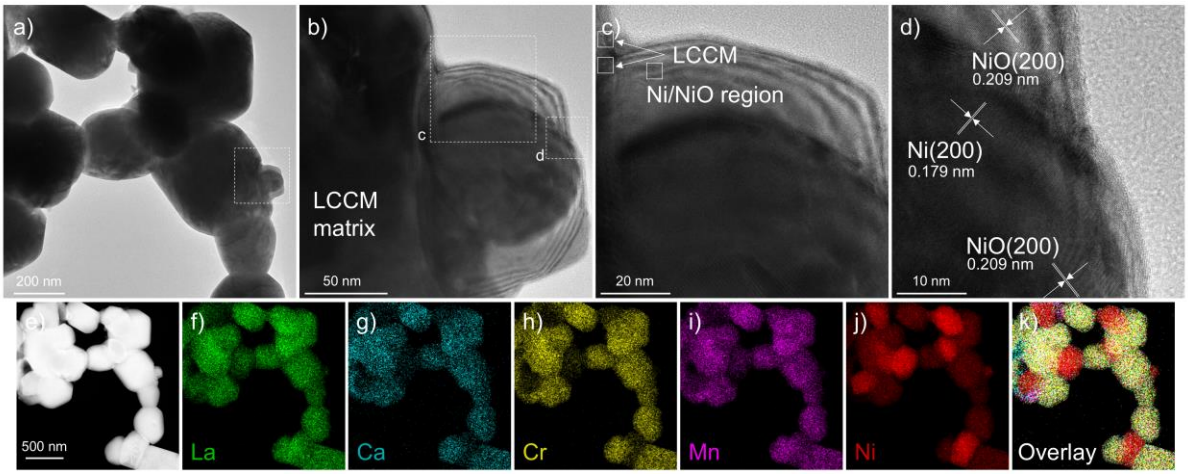

Fig. S8. (a–d) TEM, HRTEM, and STEM-EDS analysis of the 150Ni–LCCM catalyst. (a) Low-magnification TEM image showing aggregated particle morphology. (b) Enlarged TEM image of the dashed region in (a), showing a Ni-containing region at the LCCM matrix interface. (c) HRTEM image enlarged from the left dashed box in (b), where lattice fringes assigned to NiO(200) and the LCCM matrix are observed in the interfacial region. (d) HRTEM image enlarged from the right dashed box in (b), showing the coexistence of NiO(200) and Ni(200) at the interfacial region. (e–k) STEM-EDS elemental mapping of the selected region: (e) HAADF image, (f) La, (g) Ca, (h) Cr, (i) Mn, (j) Ni, and (k) corresponding elemental overlay.

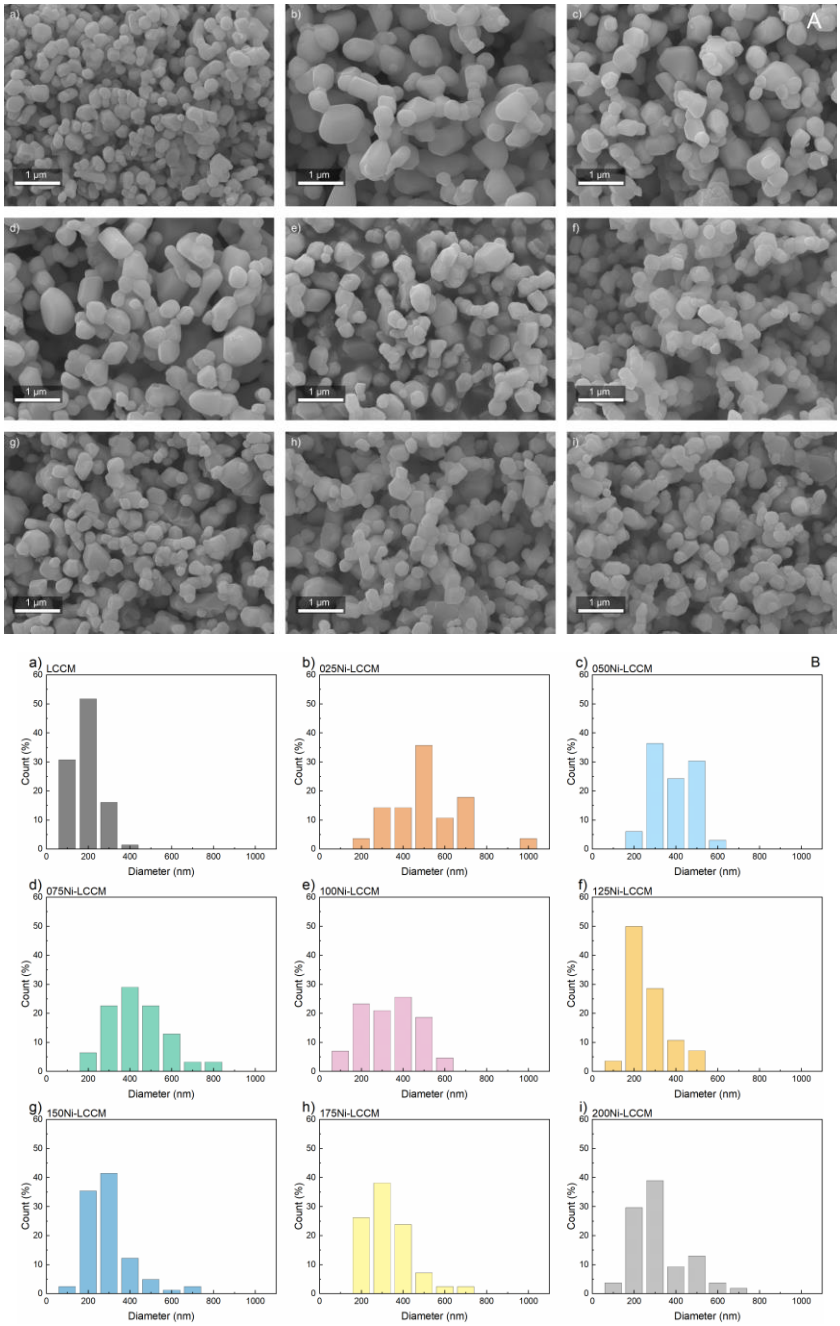

Fig. S9. Representative FESEM images (A) and corresponding particle size distributions (B) of LCCM and xNi-LCCM catalysts (x = 025–200). In panel A: (a) LCCM, (b) 025Ni-LCCM, (c) 050Ni-LCCM, (d) 075Ni-LCCM, (e) 100Ni-LCCM, (f) 125Ni-LCCM, (g) 150Ni-LCCM, (h) 175Ni-LCCM, and (i) 200Ni-LCCM. Panel B shows the corresponding particle size distributions in the same order: (a) LCCM, (b) 025Ni-LCCM, (c) 050Ni-LCCM, (d) 075Ni-LCCM, (e) 100Ni-LCCM, (f) 125Ni-LCCM, (g) 150Ni-LCCM, (h) 175Ni-LCCM, and (i) 200Ni-LCCM. Particle sizes were determined using the maximum Feret diameter and plotted as normalized frequency with identical binning across all samples. Images were acquired at 20,000× magnification (scale bar: 1 µm).

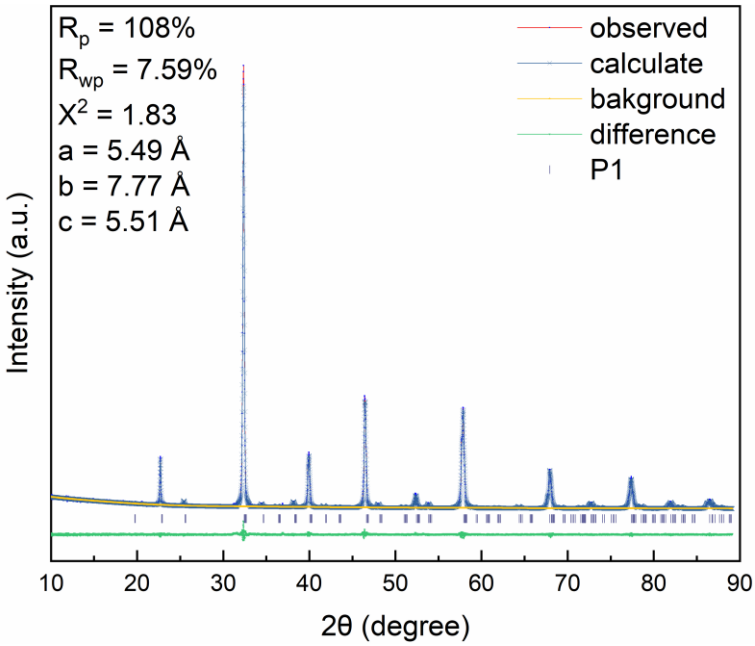

Fig. S10. XRD pattern and corresponding Rietveld refinement of LCCM, showing observed, calculated, and difference profiles.

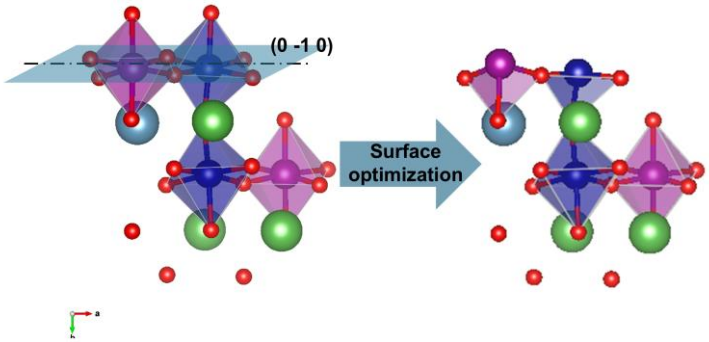

Fig. S11. LCCM surface model used for DFT calculations, constructed based on XRD Rietveld refinement.

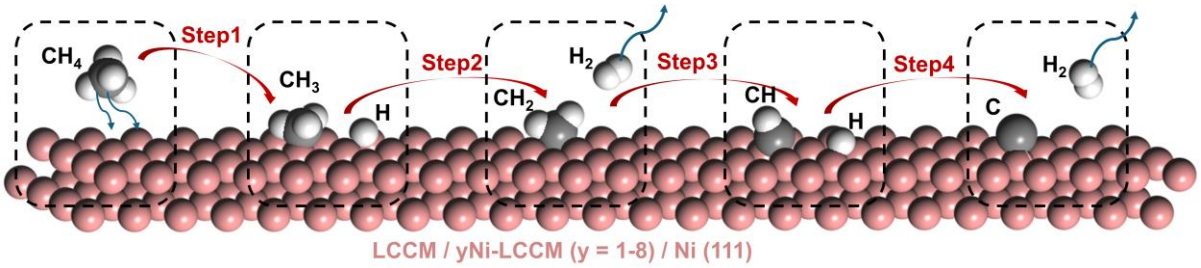

Fig. S12. Schematic illustration of the elementary C–H bond cleavage steps considered in the DFT calculations for methane decomposition on LCCM, yNi–LCCM, and Ni(111) surfaces. Hydrogen recombination/desorption is shown schematically for completeness but was not used to define the rate-limiting activation barriers.

REFERENCES

1. Pudukudy, M.; Yaakob, Z.; Mazuki, M. Z.; Takriff, M. S.; Jahaya, S. S. One-Pot Sol-Gel Synthesis of MgO Nanoparticles Supported Nickel and Iron Catalysts for Undiluted Methane Decomposition into COx Free Hydrogen and Nanocarbon. Appl. Catal. B: Environ. 2017, 218, 298–316. DOI
2. Choi, J. B.; Im, J. S.; Kang, S. C.; Lee, Y.-S.; Lee, C.-W. Effect of Metal–Support Interaction in Ni/SiO2 Catalysts on the Growth of Carbon Nanotubes by Methane Decomposition. Carbon Lett. 2023, 33, 477–488. DOI
3. Nasir Uddin, Md.; Wan Daud, W. M. A.; Abbas, H. F. Co-Production of Hydrogen and Carbon Nanofibers from Methane Decomposition over Zeolite Y Supported Ni Catalysts. Energy Convers. Manag. 2015, 90, 218–229. DOI
4. Kosari, M.; Portillo, S. B.; Xi, S.; Pedersen, A.; Talpade, A.; Li, F. Zr-Promoted Ni Nanoparticles in Mesoporous Silica Spheres (NiZr/mSiO2) for Catalytic Decomposition of Methane. Chem. Eng. J. 2025, 507, 160328. DOI
5. Ahmad, A.; Pillantakath, A. R.; Shoaibi, A. A.; Srinivasakannan, C.; Hossain, M. M. Enhanced Methane Decomposition over Ni-Co/MCM-41 Catalysts: Effect of Co Doping on Activity, Stability, and Carbon Morphology. Energy Convers. Manag.: X 2025, 28, 101381. DOI
6. Maneerung, T.; Hidajat, K.; Kawi, S. Co-Production of Hydrogen and Carbon Nanofibers from Catalytic Decomposition of Methane over LaNi(1−x)Mx O3−α Perovskite (Where M = Co, Fe and X = 0, 0.2, 0.5, 0.8, 1). Int. J. Hydrog. Energy 2015, 40, 13399–13411. DOI
7. Pinilla, J. L.; Utrilla, R.; Lázaro, M. J.; Moliner, R.; Suelves, I.; García, A. B. Ni- and Fe-Based Catalysts for Hydrogen and Carbon Nanofilament Production by Catalytic Decomposition of Methane in a Rotary Bed Reactor. Fuel Process. Technol 2011, 92, 1480–1488. DOI
8. Wang, D.; Li, W.; Liu, J.; Gao, Z.; Xu, G.; Cui, Y. Methane Thermocatalytic Decomposition to COx-Free Hydrogen and Carbon Nanomaterials over Ni–Mn–Ru/Al2O3 Catalysts. Int. J. Hydrog. Energy 2020, 45, 30431–30442. DOI